Designing the Morphology of Separated Phases in Multicomponent Liquid Mixtures

Sheng Mao,[1,2] Milena S. Chakraverti-Wuerthwein,[3] Hunter Gaudio,[2,4] and Andrej Košmrlj[2,5,*]
[1]Department of Mechanics and Engineering Science, BIC-ESAT, College of Engineering, Peking University, Beijing 100871, People's Republic of China
[2]Department of Mechanical and Aerospace Engineering, Princeton University, Princeton, New Jersey 08544, USA
[3]Department of Physics, Princeton University, Princeton, New Jersey 08544, USA
[4]Department of Mechanical Engineering, Villanova University, Villanova, Pennsylvania 19085, USA
[5]Princeton Institute for the Science and Technology of Materials (PRISM), Princeton University, Princeton, New Jersey 08544, USA

(Received 8 July 2020; accepted 6 October 2020; published 19 November 2020)

Phase separation of multicomponent liquid mixtures plays an integral part in many processes ranging from industry to cellular biology. In many cases the morphology of coexisting phases is crucially linked to the function of the separated mixture, yet it is unclear what determines the morphology when multiple phases are present. We developed a graph theory approach to predict the topology of coexisting phases from a given set of surface energies, enumerate all topologically distinct morphologies, and reverse engineer conditions for surface energies that produce the target morphology.

DOI: 10.1103/PhysRevLett.125.218003

Phase separation and multiphase coexistence are ubiquitous ranging from the simple demixing of water and oil to more sophisticated industrial processes related to medicine, food, cosmetics, energy, environment, etc. [1]. Phase separation and multiphase coexistence also occur in nature, where they give rise to structural colors in birds [2–4] and produce a plethora of intracellular condensates [5–8].

Coexisting liquid phases can adopt a variety of morphologies [9–15], which are often directly linked to some function, e.g., the nested morphology of separated phases can assist with drug delivery [16] and with the biogenesis of ribosomes inside cell nuclei [17], while the tunable morphologies of multiphase droplets can serve as microlenses with tunable focal length [14]. The control of the morphology of separated liquid phases could open the avenue for new applications, but we currently lack tools for designing the morphology of more than three coexisting phases. In this Letter we make an important step in this direction.

The phase separation process is rooted in thermodynamics and the main principles have been known since Gibbs [18]. More recently these arguments have been extended to multicomponent systems and several tools have been developed that enable predicting the number of coexisting phases, their compositions and volume fractions, and surface energies between them by minimizing the bulk free energy [19–25]. To determine how these phases arrange in space, we also need to minimize the surface energies. Here, we neglect buoyancy effects, hydrodynamics, and chemical reactions, which can also affect the morphology [1,7,26].

The focus of this Letter is to explain how surface energies determine the topology of separated liquid phases, which can be represented with a connectivity graph, and we also briefly comment how volume fractions affect the geometry of separated phases. We show how to use graph theory to predict the topology of separated phases from a given set of surface energies (forward problem), enumerate all topologically distinct morphologies, and reverse engineer conditions for surface energies that produce the target morphology (inverse problem).

The graph theory approach presented below is general and can be applied to any model system, where the surface energies can be measured experimentally or numerically. To introduce relevant concepts, we first discuss the morphology of three coexisting phases R (red), G (green), and B (blue), with surface energies $\gamma_{RB} \geq \gamma_{RG} \geq \gamma_{GB} > 0$. When surface energies satisfy the triangle inequality ($\gamma_{RB} < \gamma_{RG} + \gamma_{GB}$), the phases partially wet each other. Triple junctions, where three phases meet, are stable [Fig. 1(a)]. The equilibrium angles between different phases can be obtained from the force balance of surface tensions, which is known as the Neumann construction [27]. In contrast, when surface energies do not satisfy the triangle inequality ($\gamma_{RB} > \gamma_{RG} + \gamma_{GB}$), the phase G completely wets the phases R and B to eliminate the high surface energy γ_{RB} [Fig. 1(b)]. Here, triple junctions are unstable because surface tensions γ_{RG} and γ_{GB} cannot balance the high surface tension γ_{RB} [Fig. 1(b)].

The topology of separated phases can be represented with a connectivity graph, where vertices correspond to phases and edges connect phases that share a 2D interface. Note that phases that meet only at points or 1D lines are disconnected in the graph representation. The fully connected graph describes the partial wetting case, where all phases are in contact with each other [Fig. 1(a)], while the

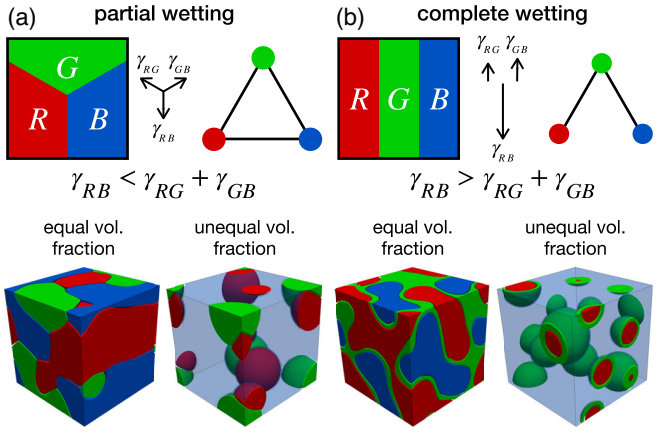

FIG. 1. Morphologies of three coexisting phases R (red), G (green), and B (blue) are determined by the magnitudes of surface tensions ($\gamma_{RB} \geq \gamma_{RG} \geq \gamma_{BG} > 0$) and volume fractions. First row: schematics of local arrangements of phases and corresponding graph representations for (a) partial wetting ($\gamma_{RB} < \gamma_{RG} + \gamma_{GB}$), and (b) complete wetting ($\gamma_{RB} > \gamma_{RG} + \gamma_{GB}$). Second row: representative simulation snapshots at 10^6 time steps (see Video S1 for the time evolution [28]). The blue phase is semitransparent for the snapshots with unequal volume fractions. The simulation parameters are given in Table S1 [28].

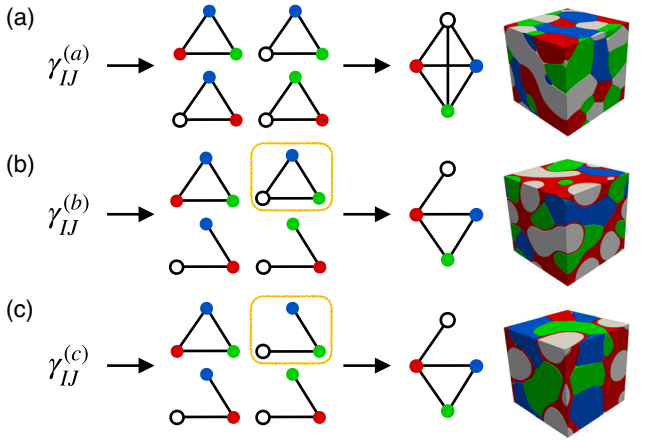

FIG. 2. Prediction of the topology of separated phases from the set of surface energies $\{\gamma_{IJ}\}$. Surface energies are used to produce the set of graphs of triplets of phases, from which we construct the connectivity graph describing the topology of separated phases (see text). (a) When all four triplet connectivity graphs are fully connected, then the connectivity graph with four vertices is also fully connected. (b),(c) Different sets of graphs (yellow boxes indicate the difference) can produce the same topology of separated phases. The last column shows representative simulation snapshots at 10^6 time steps. The simulation parameters are given in Table S1 [28].

graph with a missing edge corresponds to the complete wetting case [Fig. 1(b)].

The wetting conditions presented above can be used to infer the behavior of mixtures with $N_p > 3$ coexisting phases. For any model system with N_c components, the first step is to predict the number N_p of coexisting phases, their compositions and volume fractions, and surface energies $\{\gamma_{IJ}\}$ between them by using the tools described in Refs. [19–25]. For each of the $\binom{N_p}{3}$ subsets of three phases $\{I, J, K\}$, the local arrangement of phases depends on the surface energies $\{\gamma_{IJ}, \gamma_{IK}, \gamma_{JK}\}$ and can be represented with triplet connectivity graphs (Fig. 1). The fully connected graph corresponds to the partial wetting case with stable triple junctions I-J-K, where surface energies satisfy the triangle inequality ($\gamma_{IJ} < \gamma_{IK} + \gamma_{JK}$, $\gamma_{IK} < \gamma_{IJ} + \gamma_{JK}$, $\gamma_{JK} < \gamma_{IJ} + \gamma_{IK}$). The graph with a missing edge I-J describes the case where the phase K completely wets the phases I and J and surface energies satisfy the inequality $\gamma_{IJ} > \gamma_{IK} + \gamma_{JK}$. Analogously we can interpret the two other graphs with either a missing edge I-K or a missing edge J-K.

The information from the triplet connectivity graphs for each of the $\binom{N_p}{3}$ subsets of three phases is then used to construct the connectivity graph for the whole system with N_p phases. Starting with a fully connected graph with N_p vertices, we iterate over each of the $\binom{N_p}{3}$ triplet graphs and for each missing edge, we remove the corresponding edge in the N_p connectivity graph. This construction is based on the *local* minimization of surface free energies. The resulting connectivity graph describes the topology of the mixture, assuming that the mixture was initially well mixed, such that during the early stages of phase separation all possible pairs of phases come in contact. See the Supplemental Material for details [28].

Figure 2 shows a few representative cases for mixtures with $N_p = 4$ coexisting phases (red, green, blue, white), where $\binom{4}{3} = 4$ triplet connectivity graphs are used to construct the connectivity graph with four vertices that describes the topology of separated phases. When all four triplet connectivity graphs are fully connected, then the connectivity graph with four vertices is also fully connected [Fig. 2(a)]. Distinct sets of triplet graphs can construct the same four-component connectivity graph. One such example can be seen in Figs. 2(b) and 2(c), where the graph is missing an edge between the white and blue and between the white and green phases because the red phase completely wets the white and blue and white and green phases. The different wetting conditions [highlighted in Figs. 2(b) and 2(c)] between the white, green, and blue phases in these distinct cases do not affect the final connectivity graph (or topology), but they affect the transient dynamics. For the case in Fig. 2(b), the white, green, and blue phases form stable triple junctions, which get broken once the red phase comes along and separates the white phase from the green and blue phases. In contrast, for the case in Fig. 2(c), the green phase completely wets the white and blue phases, but the presence of the red phase separates the green and white phases.

To demonstrate how the graph theory representation applies to a specific model system, we use the

Flory-Huggins [36,37] model of regular solutions together with a Cahn-Hilliard approach for kinetics and interfacial energies [29] for $N_p = 3$, 4, and 5 coexisting phases in 3D. The free energy density f of the mixture with N_c different components is written as [7,25,38]

$$\frac{f}{cRT} = \sum_{i=1}^{N} \phi_i \ln \phi_i + \frac{1}{2} \sum_{i,j=1}^{N} \chi_{ij} \phi_i \phi_j - \frac{\lambda^2}{2} \sum_{i,j=1}^{N} \chi_{ij} \nabla \phi_i \nabla \phi_j, \quad (1)$$

where c is the total concentration of the mixture, R the gas constant, T the temperature, ϕ_i the volume fraction of the component i with $\sum_i \phi_i = 1$, χ_{ij} the interaction parameter between components i and j with $\chi_{ii} = 0$, and λ is the characteristic width of the interface. In Eq. (1) the three terms describe the entropy of mixing, the interaction energy, and the interfacial energy [39]. The volume fractions evolve as

$$\frac{\partial \phi_i}{\partial t} = D_i \nabla \cdot \left[\phi_i \sum_j (\delta_{ij} - \phi_j) \nabla \tilde{\mu}_j \right], \quad (2)$$

where D_i is the diffusion coefficient [40], δ_{ij} the Kronecker delta, and $\tilde{\mu}_j = 1 + \ln \phi_j + \sum_k \chi_{jk} (1 + \lambda^2 \nabla^2) \phi_k$ are the dimensionless chemical potentials. Here, we also assume that the interaction parameters χ_{ij} are sufficiently large, such that the mixture separates into $N_p = N_c$ distinct phases via spinodal decomposition, where each of the phases I is enriched with the component i [25], and the volume fractions of separated phases are approximately equal to the average volume fractions $\{\bar{\phi}_i\}$ of components. In this limit, the surface energies can be estimated as $\gamma_{IJ} \approx (\pi c \lambda RT/4) \chi_{ij}$. The details of the simulations are provided in the Supplemental Material [28] and Ref. [25].

In Figs. 1 and 2 we checked that the connectivity graphs accurately predict the topology of separated phases in simulations with $N_c = 3$ and $N_c = 4$ components, respectively, where the interaction parameters $\chi_{ij} \propto \gamma_{IJ}$ were chosen to be consistent with the set of inequalities for surface energies described by the graphs of triplets of phases. Note that the topology of separated phases is fully determined by surface tensions, while the geometry of separated phases also depends on the volume fractions of phases (Fig. 1). Phases percolate through the whole space, when their volume fractions exceed the percolation threshold (≈0.34 in 3D [41]), but otherwise they break into droplets to minimize the surface energy, which is known as the Rayleigh-Plateau instability [27,42].

The representation of the topology of separated phases in terms of the connectivity graphs enables us to enumerate all topologically distinct morphologies, which correspond to all connected unlabeled graphs [43]. For $N_p = 3$ phases there are two distinct graphs, which are shown in Fig. 1. For $N_p = 4$ phases there are six distinct graphs (Fig. 3), which can all be realized by appropriately adjusting surface energies (as described below). Since some of the topologies can be obtained from multiple sets of graphs for triplets of phases [Figs. 2(b) and 2(c)], we systematically investigated all possibilities for the mixture with $N_p = 4$ phases.

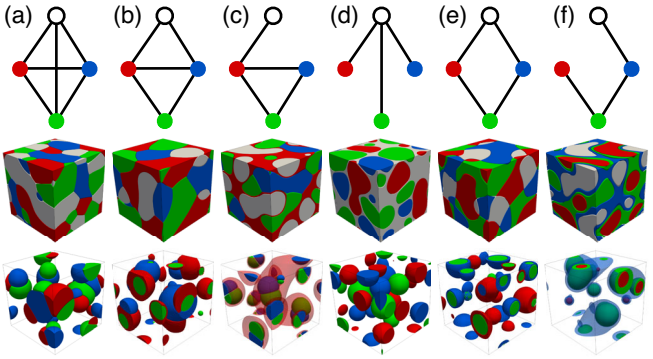

FIG. 3. Graph representations and simulation snapshots at 10^6 time steps for all (a)–(f) six distinct topologies of four coexisting phases with equal volume fractions (top) and nonequal volume fractions with transparent white phase (bottom). See Video S2 for time evolution [28]. The simulation parameters are given in Table S1 [28].

First we generated all $4^{\binom{N_p}{3}} = 4^4 = 256$ sets of $\binom{N_p}{3} = 4$ triplet connectivity graphs, where each graph can either be fully connected or is missing one of the three edges. Then we removed all duplicate sets of graphs that can be obtained by permutations of labels, resulting in 19 distinct sets of graphs (Figs. S1, S2 [28]). Each set of graphs of triplet phases corresponds to a set of inequalities for surface energies $\{\gamma_{IJ}\}$ as described above, which can have either infinite solutions or no solutions. We found that 6 of the 19 sets have no solutions (Figs. S2 [28]). To obtain representative values of interaction parameters $\{\chi_{ij}\}$ for the other 13 sets (Figs. S1 [28]), we solved a linear programming problem by minimizing the sum $\sum_{ij} \chi_{ij}$ subject to the inequalities provided by the set of graphs, where we took into account that $\chi_{ij} \propto \gamma_{IJ}$. To ensure that the inequalities were strictly enforced we added a small $\epsilon = 0.2$–0.5 to each inequality, e.g., $\chi_{ij} \geq \epsilon + \chi_{ik} + \chi_{jk}$. Furthermore, we imposed additional constraints $\chi_{ij} \geq \chi_{\min} = 2$–$3$, where $\chi_{\min}$ has to be sufficiently large to ensure that the mixture actually separates into four phases via spinodal decomposition [25].

This way we were able to obtain representative simulations for all 13 distinct sets of graphs (Fig. S1 [28]) and the topologies of separated phases were consistent with predictions from the graph theory approach described above. These 13 cases can be grouped in 6 distinct topologies, which are shown in Fig. 3 (see Video S2 for time evolution [28]), where we also show how changes in volume fraction of phases change the geometry, but not the topology of separated phases (Note that the morphologies in 2D and 3D are equivalent (Fig. S3 [28]).) In Fig. 3(e) we observed stable quadruple junctions, where all four phases meet [44]. While quadruple junctions are typically

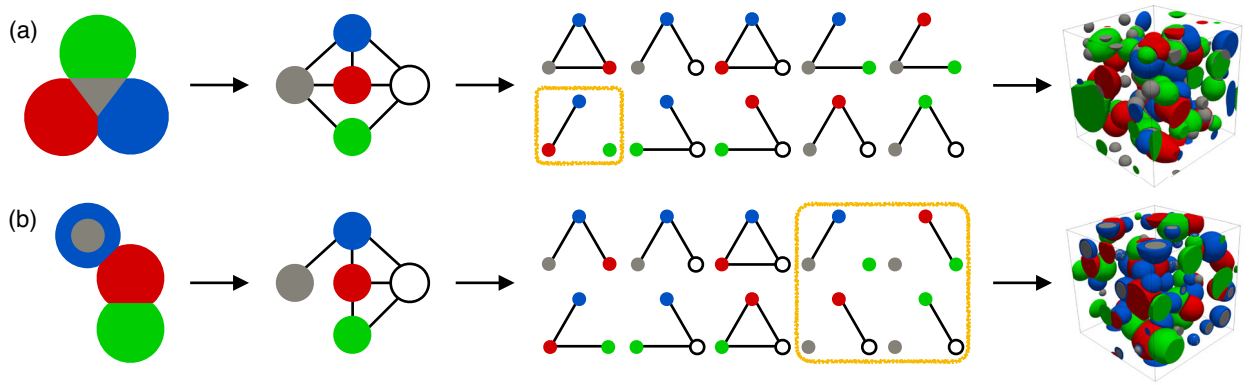

FIG. 4. Reverse engineering of (a), (b) two target structures. To reverse engineer the model parameters for target structures, we first construct a connectivity graph, which is then divided into subgraphs of triplets of phases that are associated with inequalities of surface energies. The subgraphs highlighted with yellow boxes do not provide any constraints on surface energies. The linear programming is used to find a set of surface energies that satisfy these inequalities (see text), which are then converted to interaction parameters χ_{ij}. The average volume fractions $\{\bar{\phi}_i\}$ of components are chosen such that the volume fractions of separated phases are consistent with the target structure. The resulting simulation snapshots at 4×10^5 time steps are shown on the right (see Video S3 for time evolution [28]). The simulation parameters are given in Table S1 [28].

energetically unstable, we show that for this case the conditions for surface tensions are such that they stabilize the quadruple junctions (Fig. S4 [28]).

The number of distinct topologies (i.e., the number of connected unlabeled graphs) rapidly increases with the number N_p of coexisting phases and scales as $e^{\alpha N_p^2}$, where $\alpha \sim 0.3$ [43]. It remains unclear whether all of them can be realized by appropriately tuning the values of $\binom{N_p}{2}$ surface energies.

Finally, we comment on how to reverse engineer surface energies to obtain target structures. Figure 4 sketches the procedure for two target morphologies with $N_p = 5$ coexisting phases. Starting from a target structure, we construct the connectivity graph, where vertices correspond to phases and edges connect phases that share a 2D interface. The connectivity graph can then be broken down into $\binom{N_p}{3} = 10$ subgraphs for triplets of phases. Each connected subgraph with three edges (partial wetting) or two edges (complete wetting) can be translated to the inequalities for surface energies as described above. However, there could also be disconnected subgraphs with only one edge or no edges (highlighted with yellow boxes in Fig. 4), which do not provide any restrictions on surface energies. For the case in Fig. 4(a) the nine subgraphs provide enough conditions on surface tensions to generate the target connectivity graph with five vertices and no additional constraints are needed for the red-green-blue subgraph. However, for the case in Fig. 4(b) the six subgraphs are not sufficient and we need to impose another restriction to ensure that the edge between the green and dark gray phases is removed, e.g., by requiring that the red (R) phase wets the green (G) and dark gray (D) phases ($\gamma_{GD} > \gamma_{RG} + \gamma_{RD}$). The set of surface energies can then be obtained by solving the linear programming problem subject to the inequalities imposed by the subgraphs and any other constraints provided by the model or experimental system. The next step is to convert the values of surface energies to interaction parameters between components. This is in general a highly nontrivial inverse problem, but here we again use the Flory-Huggins model in the regime, where $\chi_{ij} \propto \gamma_{IJ}$. The final step is to adjust the volume fractions $\{\bar{\phi}_i\}$ for components, such that the volume fractions of separated phases are consistent with the target structure. This way we successfully constructed the model parameters to produce target structures in simulations (Fig. 4 and Video S3 [28]).

The graph theory approach based on surface energies presented here is general. It can be used to explain how cells dynamically tune the morphology of intracellular condensates [5–8]. It can be applied to any model or experimental liquid mixture, and can also be generalized to other systems, such as block copolymers [45] or liquid crystals [46] by considering the effects of surface energies. In experiments it may be challenging to find immiscible fluids with sufficiently distinct surface energies to realize some complex target structures, but the promising new avenue is the phase separation of the solution of DNA strands [47,48], where the interactions between DNA strands can be programmed via their sequences. Note that in a liquid environment separated phases continue to coarsen over time, but in some applications it may be beneficial to produce monodisperse structured droplets. Monodisperse structured droplets can be produced very efficiently with microfluidic devices [9,11,12], or by infusing a liquid mixture in a nonwetting elastomer, where the elastic deformation of the elastomer matrix can arrest the coarsening to produce monodisperse droplets [49–52]. We hope that our study will stimulate further theoretical and experimental investigation of phase separation of multicomponent liquid mixtures in a wide range of fields.

This research was primarily supported by NSF through the Princeton University Materials Research Science and Engineering Center DMR-1420541 and through the Research Experiences for Undergraduates (REU) Site EEC-1559973. We would like to acknowledge useful discussions with Mikko Haataja, Yaofeng Zhong, Howard Stone, Ned Wingreen, Moumita Das, and Xiaoting Sun.

S. M. and M. S. C-W. contributed equally to this work.

*andrej@princeton.edu

[1] D. Lohse and X. Zhang, Physicochemical hydrodynamics of droplets out of equilibrium, Nat. Rev. Phys. **2**, 426 (2020).
[2] E. R. Dufresne, H. Noh, V. Saranathan, S. G. J. Mochrie, H. Cao, and R. O. Prum, Self-assembly of amorphous biophotonic nanostructures by phase separation, Soft Matter **5**, 1792 (2009).
[3] A. J. Parnell, A. L. Washington, O. O. Mykhaylyk, C. J. Hill, A. Bianco, S. L. Burg, A. J. C. Dennison, M. Snape, A. J. Cadby, A. Smith *et al.*, Spatially modulated structural colour in bird feathers, Sci. Rep. **5**, 18317 (2015).
[4] S. L. Burg and A. J. Parnell, Self-assembling structural colour in nature, J. Phys. Condens. Matter **30**, 413001 (2018).
[5] A. A. Hyman, C. A. Weber, and F. Jülicher, Liquid-liquid phase separation in biology, Annu. Rev. Cell Dev. Biol. **30**, 39 (2014).
[6] Y. Shin and C. P. Brangwynne, Liquid phase condensation in cell physiology and disease, Science **357**, eaaf4382 (2017).
[7] J. Berry, C. P. Brangwynne, and M. Haataja, Physical principles of intracellular organization via active and passive phase transitions, Rep. Prog. Phys. **81**, 046601 (2018).
[8] J.-M. Choi, A. S. Holehouse, and R. Pappu, Physical principles underlying the complex biology of intracellular phase transitions, Annu. Rev. Biophys. **49** (2020).
[9] A. S. Utada, E. Lorenceau, D. R. Link, P. D. Kaplan, H. A Stone, and D. A. Weitz, Monodisperse double emulsions generated from a microcapillary device, Science **308**, 537 (2005).
[10] K.-H. Roh, D. C. Martin, and J. Lahann, Triphasic nanocolloids, J. Am. Chem. Soc. **128**, 6796 (2006).
[11] R. K. Shah, H. Cheung Shum, A. C. Rowat, D. Lee, J. J. Agresti, A. S. Utada, L.-Y. Chu, J.-W. Kim, A. Fernandez-Nieves, C. J. Martinez, and D. A. Weitz, Designer emulsions using microfluidics, Mater. Today **11**, 18 (2008).
[12] C.-H. Choi, D. A. Weitz, and C.-S. Lee, One step formation of controllable complex emulsions: From functional particles to simultaneous encapsulation of hydrophilic and hydrophobic agents into desired position, Adv. Mater. **25**, 2536 (2013).
[13] L. D Zarzar, V. Sresht, E. M. Sletten, J. A. Kalow, D. Blankschtein, and T. M. Swager, Dynamically reconfigurable complex emulsions via tunable interfacial tensions, Nature (London) **518**, 520 (2015).
[14] S. Nagelberg, L. D. Zarzar, N. Nicolas, K. Subramanian, J. A. Kalow, V. Sresht, D. Blankschtein, G. Barbastathis, M. Kreysing, T. M. Swager, and M. Kolle, Reconfigurable and responsive droplet-based compound micro-lenses, Nat. Commun. **8**, 14673 (2017).
[15] P. G. Moerman, P. C. Hohenberg, E. Vanden-Eijnden, and J. Brujić, Emulsion patterns in the wake of a liquid–liquid phase separation front, Proc. Natl. Acad. Sci. U.S.A. **115**, 3599 (2018).
[16] M. F. Haase and J. Brujić, Tailoring of high-order multiple emulsions by the liquid–liquid phase separation of ternary mixtures, Angew. Chem. Int. Ed. **53**, 11793 (2014).
[17] M. Feric, N. Vaidya, T. S. Harmon, D. M. Mitrea, L. Zhu, T. M. Richardson, R. W. Kriwacki, R. V. Pappu, and C. P. Brangwynne, Coexisting liquid phases underlie nucleolar subcompartments, Cell **165**, 1686 (2016).
[18] J. W. Gibbs, On the equilibrium of heterogeneous substances, Trans. Conn. Acad. Arts Sci. **3**, 108 (1875).
[19] A. Z. Panagiotopoulos, Direct determination of phase coexistence properties of fluids by Monte Carlo simulation in a new ensemble, Mol. Phys. **61**, 813 (1987).
[20] A. Z. Panagiotopoulos, N. Quirke, M. Stapleton, and D. J. Tildesley, Phase equilibria by simulation in the Gibbs ensemble: Alternative derivation, generalization and application to mixture and membrane equilibria, Mol. Phys. **63**, 527 (1988).
[21] D. Frenkel and B. Smit, *Understanding Molecular Simulation: From Algorithms to Applications*, 2nd ed. (Elsevier, New York, 2002).
[22] T. Cool, A. Bartol, M. Kasenga, K. Modi, and R. E. García, Gibbs: Phase equilibria and symbolic computation of thermodynamic properties, CALPHAD: Comput. Coupling Phase Diagrams Thermochem. **34**, 393 (2010).
[23] P. Koukkari and R. Pajarre, A Gibbs energy minimization method for constrained and partial equilibria, Pure Appl. Chem. **83**, 1243 (2011).
[24] J. Wolff, C. M. Marques, and F. Thalmann, Thermodynamic Approach to Phase Coexistence in Ternary Phospholipid-Cholesterol Mixtures, Phys. Rev. Lett. **106**, 128104 (2011).
[25] S. Mao, D. Kuldinow, M. P. Haataja, and A. Košmrlj, Phase behavior and morphology of multicomponent liquid mixtures, Soft Matter **15**, 1297 (2019).
[26] T. Koga and K. Kawasaki, Spinodal decomposition in binary fluids: Effects of hydrodynamic interactions, Phys. Rev. A **44**, R817(R) (1991).
[27] P.-G. de Gennes, F. Brochard-Wyart, and D. Quéré, *Capillarity and Wetting Phenomena: Drops, Bubbles, Pearls, Waves* (Springer Science & Business Media, New York, 2013).
[28] See Supplemental Material at http://link.aps.org/supplemental/10.1103/PhysRevLett.125.218003 for the justification for the graph approach to predict the topology of the mixture and simulation details, which includes Refs. [25,29–35].
[29] J. W. Cahn and J. E. Hilliard, Free energy of a nonuniform system. I. Interfacial free energy, J. Chem. Phys. **28**, 258 (1958).
[30] P. C. Hohenberg and B. I. Halperin, Theory of dynamic critical phenomena, Rev. Mod. Phys. **49**, 435 (1977).
[31] E. J. Kramer, P. Green, and C. J. Palmstrøm, Interdiffusion and marker movements in concentrated polymer-polymer diffusion couples, Polymer **25**, 473 (1984).

[32] J. Zhu, L.-Q. Chen, J. Shen, and V. Tikare, Coarsening kinetics from a variable-mobility Cahn-Hilliard equation: Application of a semi-implicit Fourier spectral method, Phys. Rev. E **60**, 3564 (1999).
[33] U. M. Ascher, S. J. Ruuth, and R. J. Spiteri, Implicit-explicit runge-kutta methods for time-dependent partial differential equations, Applied Numerical Mathematics **25**, 151 (1997).
[34] J. W. Cooley, P. A. W. Lewis, and P. D. Welch, The fast Fourier transform and its applications, IEEE Trans. Ed. **12**, 27 (1969).
[35] J. Ahrens, B. Geveci, and C. Law, Paraview: An end-user tool for large data visualization, in *The Visualization Handbook*, edited by C. D. Hansen and C. R. Johnson (Elsevier, New York, 2005), pp. 717–731.
[36] M. L. Huggins, Solutions of long chain compounds, J. Chem. Phys. **9**, 440 (1941).
[37] P. J. Flory, Thermodynamics of high polymer solutions, J. Chem. Phys. **10**, 51 (1942).
[38] J. J. Hoyt, The continuum theory of nucleation in multicomponent systems, Acta Metall. Mater. **38**, 1405 (1990).
[39] Note that the negative sign for the interfacial energy is due to the incompressibility $\sum_i \nabla\phi_i = 0$ as discussed in [25].
[40] We assume that all components have the same diffusion coefficient $D_i \equiv D$, but the respective mobilities are different and composition-dependent. See Supplemental Material and [25] for details.
[41] D. Stauffer and A. Aharony, *Introduction to Percolation Theory* (Taylor and Francis, London, 1994).
[42] J. Eggers, Nonlinear dynamics and breakup of free-surface flows, Rev. Mod. Phys. **69**, 865 (1997).
[43] F. Harary and E. M. Palmer, *Graphical Enumeration* (Elsevier, New York, 2014).
[44] Note that for the snapshot in Fig. 3(e) the green and the white phases meet at quadruple junctions, but this is not in conflict with the connectivity graphs, where the connected vertices correspond to phases that share a 2D interface.
[45] Y. Mai and A. Eisenberg, Self-assembly of block copolymers, Chem. Soc. Rev. **41**, 5969 (2012).
[46] T. Kato, Self-assembly of phase-segregated liquid crystal structures, Science **295**, 2414 (2002).
[47] D. T. Nguyen and O. A. Saleh, Tuning phase and aging of DNA hydrogels through molecular design, Soft Matter **13**, 5421 (2017).
[48] D. T. Nguyen, B.-j. Jeon, G. R. Abraham, and O. A. Saleh, Length-dependence and spatial structure of DNA partitioning into a DNA liquid, Langmuir **35**, 14849 (2019).
[49] R. W. Style, T. Sai, N. Fanelli, M. Ijavi, K. Smith-Mannschott, Q. Xu, L. A. Wilen, and E. R. Dufresne, Liquid-Liquid Phase Separation in an Elastic Network, Phys. Rev. X **8**, 011028 (2018).
[50] J. Y. Kim, Z. Liu, B. M. Weon, T. Cohen, C.-Y. Hui, E. R. Dufresne, and R. W. Style, Extreme cavity expansion in soft solids: Damage without fracture, Sci. Adv. **6**, eaaz0418 (2020).
[51] K. A. Rosowski, T. Sai, E. Vidal-Henriquez, D. Zwicker, R. W. Style, and E. R. Dufresne, Elastic ripening and inhibition of liquid–liquid phase separation, Nat. Phys. **16**, 422 (2020).
[52] M. Kothari and T. Cohen, Effect of elasticity on phase separation in heterogeneous systems, J. Mech. Phys. Solids **145**, 104153 (2020).

Supplemental Material: Designing morphology of separated phases in multicomponent liquid mixtures

Sheng Mao,[1,2] Milena S. Chakraverti-Wuerthwein,[3] Hunter Gaudio,[2,4] and Andrej Košmrlj[2,5]

[1] *Department of Mechanics and Engineering Science, BIC-ESAT, College of Engineering, Peking University, Beijing 100871, People's Republic of China*

[2] *Department of Mechanical and Aerospace Engineering, Princeton University, Princeton, New Jersey 08544, USA*

[3] *Department of Physics, Princeton University, Princeton, New Jersey 08544, USA*

[4] *Department of Mechanical Engineering, Villanova University, Villanova, Pennsylvania, 19085, USA*

[5] *Princeton Institute for the Science and Technology of Materials (PRISM), Princeton University, Princeton, New Jersey 08544, USA*

JUSTIFICATION FOR THE GRAPH APPROACH TO PREDICT THE TOPOLOGY OF THE MIXTURE

In the main text we described how the set of surface energies $\{\gamma_{IJ}\}$ can be used to predict the topology of the mixture via the graph approach. Here, we repeat the procedure and provide the justification based on the *local* minimization of surface free energies, where we assume that the mixture was initially well mixed, such that during the early stages of phase separation all possible pairs of phases come in contact.

For each of the $\binom{N_p}{3}$ subsets of three phases $\{I, J, K\}$, the local arrangement of phases depends on the surface energies $\{\gamma_{IJ}, \gamma_{IK}, \gamma_{JK}\}$ and can be represented with triplet connectivity graphs (see Fig. 1 in main text). The fully connected graph corresponds to the partial wetting case with stable triple junctions $I-J-K$, where surface energies satisfy the triangle inequality ($\gamma_{IJ} < \gamma_{IK} + \gamma_{JK}$, $\gamma_{IK} < \gamma_{IJ} + \gamma_{JK}$, $\gamma_{JK} < \gamma_{IJ} + \gamma_{IK}$). The graph with a missing edge $I-J$ describes the case where the phase K completely wets the phases I and J and surface energies satisfy the inequality $\gamma_{IJ} > \gamma_{IK} + \gamma_{JK}$. Analogously we can interpret the two other graphs with either a missing edge $I-K$ or a missing edge $J-K$. The partial and complete wetting cases discussed above are directly related to the *local* minimization of the surface free energy for the three phases.

The wetting conditions for the $\binom{N_p}{3}$ subsets of three phases are then used to construct the connectivity graph for the whole mixture consisting of N_p phases. If the phases I and J are completely wet by any other phase K ($\gamma_{IJ} > \gamma_{IK} + \gamma_{JK}$), then such phases I and J are also not in contact in the mixture consisting of N_p phases, otherwise the surface free energy could be lowered by inserting a small volume of the phase K in between them as indicated on the sketch below.

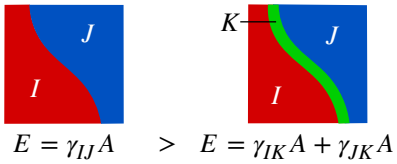

Such phases I and J are thus disconnected in the connectivity graph. In contrast, if the phases I and J are partially wet by all the other phases, which means that the phases I and J form stable triple junctions with any other phase, then they are expected to be connected in the connectivity graph. If the mixture was initially well mixed, then it is very likely that the phases I and J will meet another phase and form a stable triple junction, which will force the phases I and J to remain in contact.

Based on the discussion above the connectivity graph that represents the topology of the mixture can be described in the following way. Starting with a fully connected graph with N_p vertices, we iterate over each of the $\binom{N_p}{3}$ triplet graphs and for each missing edge (complete wetting), we remove the corresponding edge in the N_p connectivity graph.

While we don't have a rigorous proof, we expect that the construction of the connectivity graph based on the physical arguments described above will in most cases describe the topology of well-mixed systems in local equilibrium. However, it might be possible that there exist some special cases for which the topology of the mixture is different from the predicted connectivity graph, e.g. if two phases are initially located in different corners of the container they may not come in contact on the relevant timescales.

SIMULATION METHODS

Here, we briefly summarize numerical simulations, which are based on the code that was developed for our previous work [1]. The volume fraction fields $\{\phi_i(\boldsymbol{x})\}$ evolve via a so-called model B or Cahn–Hilliard dynamics [2, 3]:

$$\frac{\partial \phi_i}{\partial t} = \nabla \cdot \left[\sum_j \tilde{M}_{ij} \nabla \tilde{\mu}_j \right], \tag{1}$$

where we introduced the dimensionless chemical potentials $\tilde{\mu}_j = 1 + \ln \phi_j + \sum_{k=1}^{N} \chi_{jk}(1 + \lambda^2 \nabla^2)\phi_k$. We adopted the Kramer's model [4] for the normalized Onsager mobility coefficients $\tilde{M}_{ij} = D_{ij}\left(\phi_i \delta_{ij} - \phi_i \phi_j\right)$ to enforce the constraint $\sum_i \phi_i = 1$. When all components have identical diffusion coefficient $D_{ij} \equiv D$, then the Eq. (1) can be re-written as

$$\frac{\partial \phi_i}{\partial t} = D \nabla \cdot \left[\phi_i \sum_j \left(\delta_{ij} - \phi_j\right) \nabla \tilde{\mu}_j \right]. \tag{2}$$

Note that there are only $N-1$ independent volume fractions and $N-1$ independent chemical potentials. Note also that the interaction parameters $\{\chi_{ij}\}$ need to satisfy the condition $\sum_{i,j=1}^{N} a_i \chi_{ij} a_j < 0$ for any $\{a_i\}$ with $\sum_{i=1}^{N} a_i = 0$ to ensure the stability of interfaces [1].

The nonlinear partial differential equations in Eqn. (2) were solved numerically in a 3D cubic box with linear dimension L discretized with $128 \times 128 \times 128$ uniform grid points and periodic boundary conditions. A semi-implicit time-integration scheme [5] was used, which enabled us to use relatively large time steps. To do so, we first discretized Eqn. (2) in time and separated the implicit linear and the explicit non-linear terms following the usual IMEX (implicit-explicit) scheme [6] as

$$\frac{\phi_i^{n+1} - \phi_i^n}{\Delta t} = N_i(\phi_i^n) + L_i(\phi_i^{n+1}), \tag{3}$$

where $\phi_i^n(\boldsymbol{x})$ is the volume fraction field of component i at time step n. N_i and L_i denote the nonlinear and linear parts of the right hand side of Eqn. (2), respectively. Following the procedure in Ref. [5], we introduced an artificial linear ∇^4 term to stabilize the nonlinear term as

$$N_i(\{\phi_i\}) = D \nabla \cdot \left[\phi_i \sum_j \left(\delta_{ij} - \phi_j\right) \nabla \tilde{\mu}_j \right] + AD\lambda^2 \nabla^4 \phi_i, \tag{4}$$

$$L_i(\{\phi_i\}) = -AD\lambda^2 \nabla^4 \phi_i, \tag{5}$$

where the numerical prefactor $A = 0.5 \max\{\chi_{ij}\}$ is chosen empirically to ensure numerical stability. When evaluating nonlinear terms $N_i(\{\phi_i\})$, the products of composition fields $\phi_i^n(\boldsymbol{x})$ are carried out in real space, while the spatial derivatives are evaluated in Fourier representation $\hat{\phi}_i^n(\boldsymbol{k}) = \int_V d\boldsymbol{x}\, e^{-i\boldsymbol{k}\cdot\boldsymbol{x}} \phi_i^n(\boldsymbol{x})/V$. The Fast Fourier Transform (FFT) algorithm was used to convert back and forth between real space and Fourier space representations [7]. In Fourier space, the implicit Eq. (3) can be solved to obtain

$$\hat{\phi}_i^{n+1} = \frac{\hat{\phi}_i^n + \hat{N}_i(\phi_i^n)\Delta t}{1 + A\lambda^2 k^4 D \Delta t}, \tag{6}$$

where $\hat{\cdot}$ denotes a Fourier transform and $k = |\boldsymbol{k}|$ is the magnitude of the wave vector $\boldsymbol{k}$.

To make equations dimensionless, the lengths are measured in units of the cubic box size L and time is measured in the units of $\tau = \lambda^2/D$, which describes the characteristic time of diffusion across the interface between two phases. We chose $\lambda/L = 0.45 \times 10^{-2}$ and a time step $\Delta t = \tau/2$. For the initial conditions we set $\phi_i(\boldsymbol{x}) = \bar{\phi}_i + \eta_i(\boldsymbol{x})$, where $\eta_i(\boldsymbol{x})$ is a uniform random noise with small magnitude and 0 mean), and then the simulation runs for a total duration of $10^5 - 10^6 \tau$. The interaction parameters $\{\chi_{ij}\}$ and the average volume fractions $\{\bar{\phi}_i\}$ used in simulations are reported in Table S1.

ParaView [8] was used for visualization, where we used isovolumes to indicate phases that are enriched in one of the components: red ($\phi_1 > \phi_{\text{cutoff}}$), green ($\phi_2 > \phi_{\text{cutoff}}$), blue ($\phi_3 > \phi_{\text{cutoff}}$), white ($\phi_4 > \phi_{\text{cutoff}}$), and dark gray ($\phi_5 > \phi_{\text{cutoff}}$). The threshold volume fraction for isovolumes was set to $\phi_{\text{cutoff}} = 0.5 - 0.6$.

TABLE S1. Simulation parameters

Figure	interaction parameters	volume fractions
Fig. 1a	$\chi_{12} = \chi_{13} = \chi_{23} = 3.25$	$\{\overline{\phi}_i\} = \{0.333, 0.333, 0.334\}$
Fig. 1a	$\chi_{12} = \chi_{13} = \chi_{23} = 3.25$	$\{\overline{\phi}_i\} = \{0.15, 0.15, 0.70\}$
Fig. 1b	$\chi_{12} = \chi_{23} = 2.5, \chi_{13} = 5.5$	$\{\overline{\phi}_i\} = \{0.333, 0.333, 0.334\}$
Fig. 1b	$\chi_{12} = \chi_{23} = 2.5, \chi_{13} = 5.5$	$\{\overline{\phi}_i\} = \{0.10, 0.20, 0.70\}$
Fig. 2a	$\chi_{12} = \chi_{13} = \chi_{23} = \chi_{14} = \chi_{24} = \chi_{34} = 5.0$	$\{\overline{\phi}_i\} = \{0.25, 0.25, 0.25, 0.25\}$
Fig. 2b	$\chi_{12} = \chi_{13} = \chi_{23} = \chi_{14} = 4.0$, $\chi_{24} = \chi_{34} = 8.2$	$\{\overline{\phi}_i\} = \{0.25, 0.25, 0.25, 0.25\}$
Fig. 2c	$\chi_{12} = \chi_{13} = \chi_{23} = \chi_{14} = 4.0$, $\chi_{24} = 8.5$, $\chi_{34} = 13.0$	$\{\overline{\phi}_i\} = \{0.25, 0.25, 0.25, 0.25\}$
Fig. 3a	$\chi_{12} = \chi_{13} = \chi_{23} = \chi_{14} = \chi_{24} = \chi_{34} = 5.0$	$\{\overline{\phi}_i\} = \{0.25, 0.25, 0.25, 0.25\}$
Fig. 3a	$\chi_{12} = \chi_{13} = \chi_{23} = \chi_{14} = \chi_{24} = \chi_{34} = 5.0$	$\{\overline{\phi}_i\} = \{0.10, 0.10, 0.10, 0.70\}$
Fig. 3b	$\chi_{12} = \chi_{13} = \chi_{23} = \chi_{14} = \chi_{34} = 4.5$, $\chi_{24} = 10.0$	$\{\overline{\phi}_i\} = \{0.25, 0.25, 0.25, 0.25\}$
Fig. 3b	$\chi_{12} = \chi_{13} = \chi_{23} = \chi_{14} = \chi_{34} = 4.5$, $\chi_{24} = 10.0$	$\{\overline{\phi}_i\} = \{0.12, 0.06, 0.12, 0.70\}$
Fig. 3c	$\chi_{12} = \chi_{13} = \chi_{23} = \chi_{14} = 4.0$, $\chi_{24} = \chi_{34} = 8.2$	$\{\overline{\phi}_i\} = \{0.25, 0.25, 0.25, 0.25\}$
Fig. 3c	$\chi_{12} = \chi_{13} = \chi_{23} = \chi_{14} = 4.0$, $\chi_{24} = \chi_{34} = 8.2$	$\{\overline{\phi}_i\} = \{0.20, 0.05, 0.05, 0.70\}$
Fig. 3d	$\chi_{12} = \chi_{13} = \chi_{23} = 7.5$, $\chi_{14} = \chi_{24} = \chi_{34} = 3.5$	$\{\overline{\phi}_i\} = \{0.25, 0.25, 0.25, 0.25\}$
Fig. 3d	$\chi_{12} = \chi_{13} = \chi_{23} = 10.5$, $\chi_{14} = \chi_{24} = \chi_{34} = 5.0$	$\{\overline{\phi}_i\} = \{0.10, 0.10, 0.10, 0.70\}$
Fig. 3e	$\chi_{12} = \chi_{23} = \chi_{14} = \chi_{34} = 3.0$, $\chi_{13} = \chi_{24} = 6.5$	$\{\overline{\phi}_i\} = \{0.25, 0.25, 0.25, 0.25\}$
Fig. 3e	$\chi_{12} = \chi_{23} = \chi_{14} = \chi_{34} = 3.0$, $\chi_{13} = \chi_{24} = 6.5$	$\{\overline{\phi}_i\} = \{0.10, 0.10, 0.10, 0.70\}$
Fig. 3f	$\chi_{12} = \chi_{23} = \chi_{34} = 2.5$, $\chi_{13} = 5.5$, $\chi_{14} = 8.5$, $\chi_{24} = 6.5$	$\{\overline{\phi}_i\} = \{0.25, 0.25, 0.25, 0.25\}$
Fig. 3f	$\chi_{12} = \chi_{23} = \chi_{34} = 3.3$, $\chi_{13} = 6.9$, $\chi_{14} = 10.5$, $\chi_{24} = 7.5$	$\{\overline{\phi}_i\} = \{0.03, 0.07, 0.20, 0.70\}$
Fig. 4a	$\chi_{12} = \chi_{23} = \chi_{45} = 8.2$, $\chi_{13} = \chi_{14} = 4.0$, $\chi_{24} = \chi_{34} = \chi_{15} = \chi_{25} = \chi_{35} = 4.0$	$\{\overline{\phi}_i\} = \{0.11, 0.11, 0.11, 0.62, 0.05\}$
Fig. 4b	$\chi_{12} = \chi_{13} = \chi_{14} = \chi_{24} = \chi_{34} = \chi_{35} = 4.0$, $\chi_{23} = \chi_{15} = \chi_{45} = 8.2$, $\chi_{25} = 12.4$	$\{\overline{\phi}_i\} = \{0.11, 0.11, 0.08, 0.65, 0.05\}$
Fig. S1a	$\chi_{12} = \chi_{13} = \chi_{23} = \chi_{14} = \chi_{24} = \chi_{34} = 5.0$	$\{\overline{\phi}_i\} = \{0.25, 0.25, 0.25, 0.25\}$
Fig. S1b.1	$\chi_{12} = \chi_{13} = \chi_{23} = \chi_{34} = 4.0$, $\chi_{14} = 6.0$, $\chi_{24} = 9.0$	$\{\overline{\phi}_i\} = \{0.25, 0.25, 0.25, 0.25\}$
Fig. S1b.2	$\chi_{12} = \chi_{13} = \chi_{23} = \chi_{14} = \chi_{34} = 4.5$, $\chi_{24} = 10.0$	$\{\overline{\phi}_i\} = \{0.25, 0.25, 0.25, 0.25\}$
Fig. S1c.1	$\chi_{12} = \chi_{13} = \chi_{23} = \chi_{14} = 4.0$, $\chi_{24} = \chi_{34} = 8.2$	$\{\overline{\phi}_i\} = \{0.25, 0.25, 0.25, 0.25\}$
Fig. S1c.2	$\chi_{12} = \chi_{13} = \chi_{23} = \chi_{14} = 4.0$, $\chi_{24} = 8.5$, $\chi_{34} = 13.0$	$\{\overline{\phi}_i\} = \{0.25, 0.25, 0.25, 0.25\}$
Fig. S1d.1	$\chi_{12} = \chi_{13} = \chi_{23} = 7.5$, $\chi_{14} = \chi_{24} = \chi_{34} = 3.5$	$\{\overline{\phi}_i\} = \{0.25, 0.25, 0.25, 0.25\}$
Fig. S1d.2	$\chi_{12} = \chi_{13} = 5.2$, $\chi_{23} = 10.6$, $\chi_{14} = \chi_{24} = \chi_{34} = 2.5$	$\{\overline{\phi}_i\} = \{0.25, 0.25, 0.25, 0.25\}$
Fig. S1e.1	$\chi_{12} = \chi_{23} = \chi_{34} = 3.0$ $\chi_{13} = \chi_{24} = 6.5$, $\chi_{14} = 4.0$	$\{\overline{\phi}_i\} = \{0.25, 0.25, 0.25, 0.25\}$
Fig. S1e.2	$\chi_{12} = \chi_{14} = 3.2$, $\chi_{13} = 6.4$, $\chi_{23} = \chi_{34} = 3.0$, $\chi_{24} = 6.2$	$\{\overline{\phi}_i\} = \{0.25, 0.25, 0.25, 0.25\}$
Fig. S1e.3	$\chi_{12} = \chi_{23} = \chi_{14} = \chi_{34} = 3.0$, $\chi_{13} = \chi_{24} = 6.5$	$\{\overline{\phi}_i\} = \{0.25, 0.25, 0.25, 0.25\}$
Fig. S1f.1	$\chi_{12} = \chi_{23} = \chi_{34} = 2.5$, $\chi_{13} = 5.5$, $\chi_{14} = 8.5$, $\chi_{24} = 6.5$	$\{\overline{\phi}_i\} = \{0.25, 0.25, 0.25, 0.25\}$
Fig. S1f.2	$\chi_{12} = \chi_{23} = \chi_{34} = 2.5$, $\chi_{13} = \chi_{24} = 5.1$, $\chi_{14} = 7.7$	$\{\overline{\phi}_i\} = \{0.25, 0.25, 0.25, 0.25\}$
Fig. S1f.3	$\chi_{12} = \chi_{23} = \chi_{34} = 2.2$, $\chi_{13} = 4.6$, $\chi_{14} = 7.0$, $\chi_{24} = 9.4$	$\{\overline{\phi}_i\} = \{0.25, 0.25, 0.25, 0.25\}$

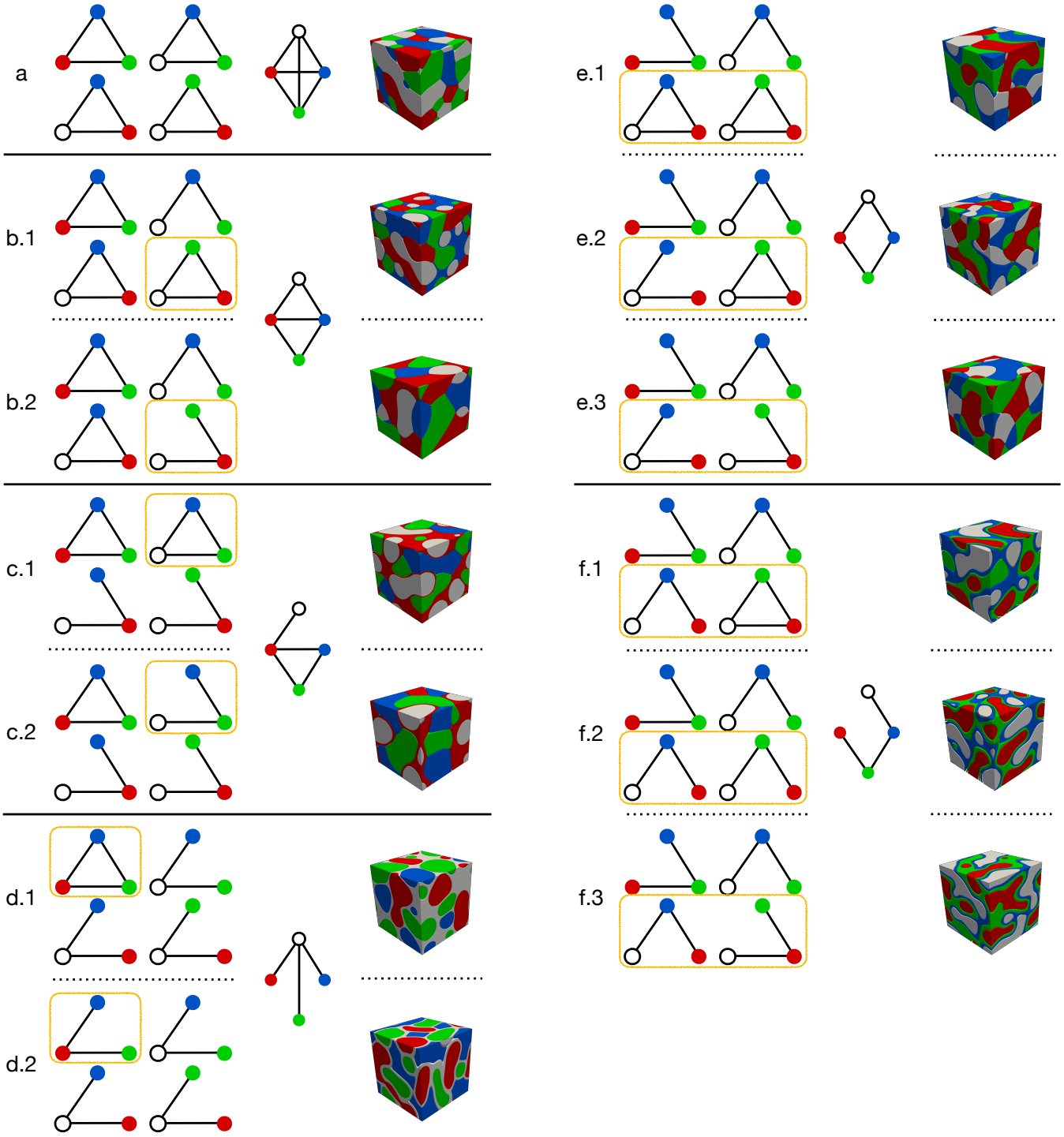

FIG. S1. All distinct sets of the wetting conditions (4 graphs of triplets) that can be realized for a mixture with $N_p = 4$ phases. These sets are grouped according to the connectivity graphs with 4 vertices describing the topology of separated phases. For each group the yellow boxes indicate the wetting conditions that differ between sets. For each set we show a simulation snapshot at 10^6 timesteps. The simulation parameters are given in Table S1.

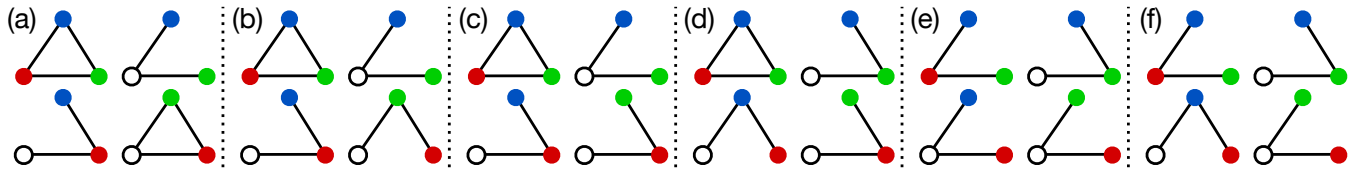

FIG. S2. All distinct sets of the wetting conditions (4 graphs of triplets) that cannot be realized for a mixture with $N_p = 4$ phases.

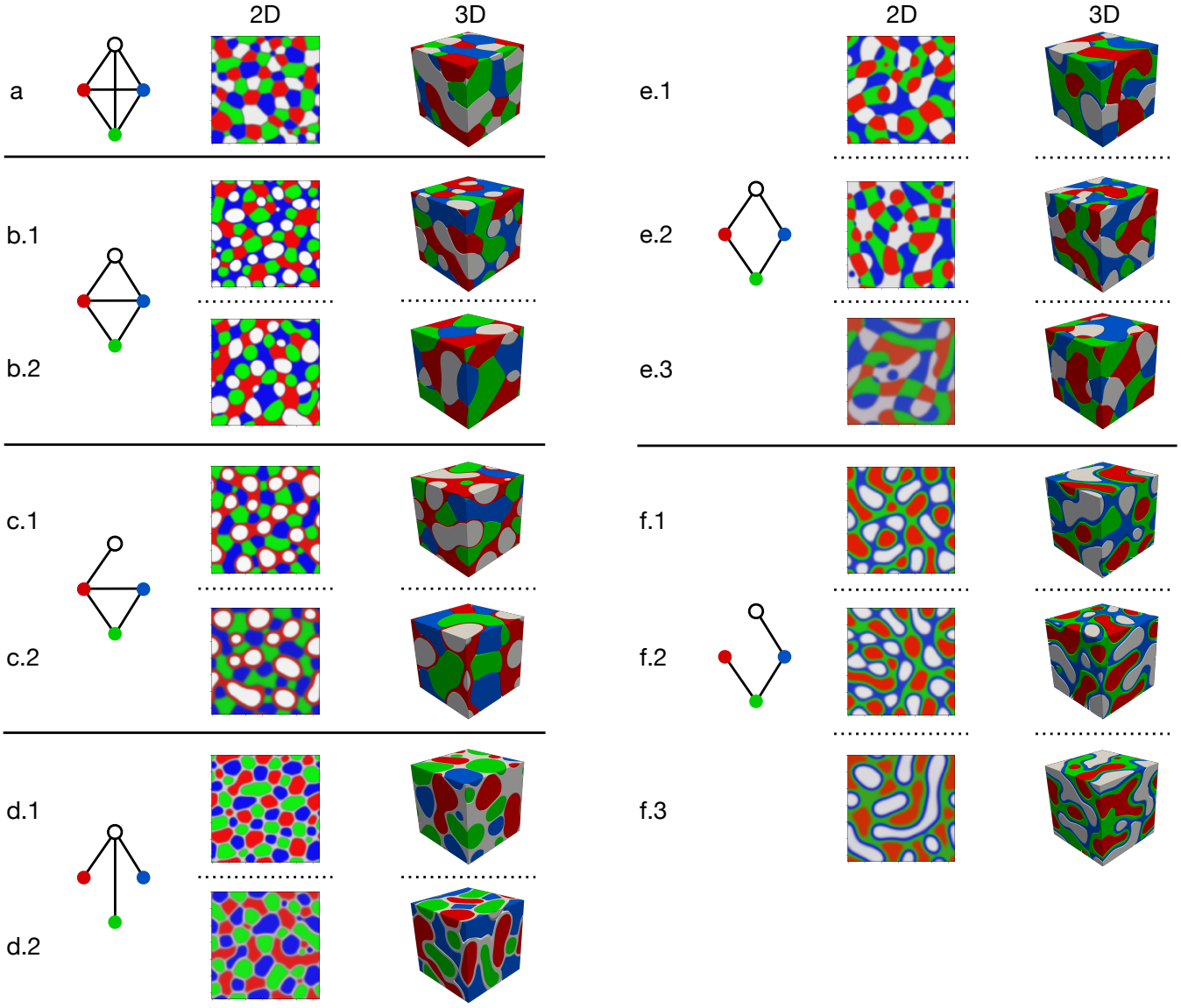

FIG. S3. Comparison of simulation snapshots in 2D and 3D for all distinct sets of the wetting conditions presented in Fig. S1. The simulation parameters are identical for 2D and 3D simulations and they are the same as in Fig. S1.

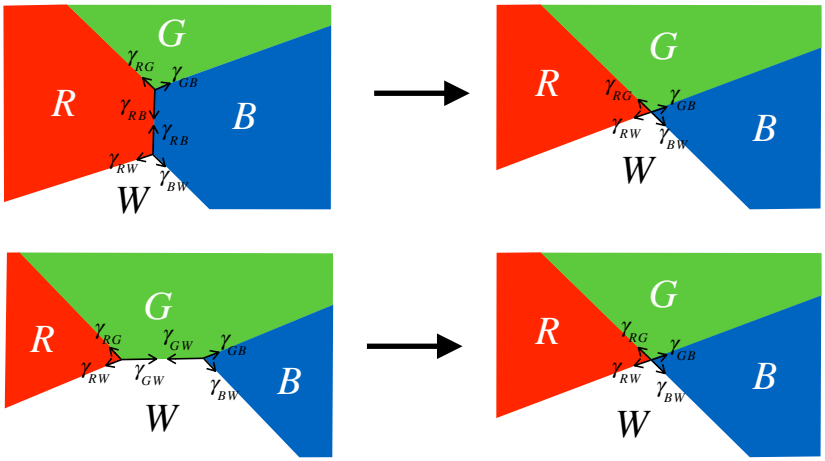

FIG. S4. Stability of quadruple junctions. For simulation snapshots in Fig. S1e the quadruple junctions are stable, because triple junctions get pulled together due to the force imbalance of surface tensions. For the case in Fig. S1e.1, the *R-G-B* junction gets pulled ($\gamma_{RB} > \gamma_{RG} + \gamma_{GB}$) toward the stable *R-B-W* junction and the *G-B-W* junction gets pulled ($\gamma_{GW} > \gamma_{GB} + \gamma_{BW}$) toward the stable *R-G-W* junction. For the case in Fig. S1e.2, the *R-G-B* and *R-B-W* junctions are pulled toward each other ($\gamma_{RB} > \gamma_{RG} + \gamma_{GB}$, $\gamma_{RB} > \gamma_{RW} + \gamma_{RG}$) and the *G-B-W* junction gets pulled ($\gamma_{GW} > \gamma_{GB} + \gamma_{BW}$) toward the stable *R-G-W* junction. For the case in Fig. S1e.3, the *R-G-B* and *R-B-W* junctions are pulled toward each other ($\gamma_{RB} > \gamma_{RG} + \gamma_{GB}$, $\gamma_{RB} > \gamma_{RW} + \gamma_{RG}$) and the *G-B-W* and *R-G-W* junctions are pulled toward each other ($\gamma_{GW} > \gamma_{GB} + \gamma_{BW}$, $\gamma_{GW} > \gamma_{GR} + \gamma_{RW}$).

[1] S. Mao, D. Kuldinow, M. P. Haataja, and A. Košmrlj, "Phase behavior and morphology of multicomponent liquid mixtures," Soft Matter **15**, 1297–1311 (2019).

[2] J. W. Cahn and J. E. Hilliard, "Free energy of a nonuniform system. I. interfacial free energy," J. Chem. Phys. **28**, 258–267 (1958).

[3] P. C. Hohenberg and B. I. Halperin, "Theory of dynamic critical phenomena," Rev. Mod. Phys. **49**, 435 (1977).

[4] E. J. Kramer, P. Green, and C. J. Palmstrøm, "Interdiffusion and marker movements in concentrated polymer-polymer diffusion couples," Polymer **25**, 473–480 (1984).

[5] J. Zhu, L.-Q. Chen, J. Shen, and V. Tikare, "Coarsening kinetics from a variable-mobility cahn-hilliard equation: Application of a semi-implicit fourier spectral method," Phys. Rev. E **60**, 3564–3572 (1999).

[6] U. M. Ascher, S. J. Ruuth, and R. J. Spiteri, "Implicit-explicit runge-kutta methods for time-dependent partial differential equations," Appl. Numer. Math. **25**, 151–167 (1997).

[7] J. W. Cooley, P. A. W. Lewis, and P. D. Welch, "The fast fourier transform and its applications," IEEE Trans. Educ. **12**, 27–34 (1969).

[8] J. Ahrens, B. Geveci, and C. Law, "Paraview: An end-user tool for large data visualization," The visualization handbook **717** (2005).